A&A, 679, A48 (2023)
https://doi.org/10.1051/0004-6361/202346448

Astronomy & Astrophysics

XMM-Newton observation of the TeV-discovered supernova remnant HESS J1534-571

N. T. Nguyen-Dang[1], G. Pühlhofer[1], M. Sasaki[2], A. Bamba[3,4,5], V. Doroshenko[1], and A. Santangelo[1]

[1] Institut für Astronomie und Astrophysik Tübingen (IAAT), Sand 1, 72076 Tübingen, Germany
e-mail: dang-thanh-nhan.nguyen@astro.uni-tuebingen.de
[2] Dr. Karl Remeis Observatory, Erlangen Centre for Astroparticle Physics, Friedrich-Alexander-Universität Erlangen-Nürnberg, Sternwartstraße 7, 96049 Bamberg, Germany
[3] Department of Physics, Graduate School of Science, The University of Tokyo, 7-3-1 Hongo, Bunkyo-ku, Tokyo 113-0033, Japan
[4] Research Center for the Early Universe, Graduate School of Science, The University of Tokyo, 7-3-1 Hongo, Bunkyo-ku, Tokyo 113-0033, Japan
[5] Trans-Scale Quantum Science Institute, The University of Tokyo, 7-3-1 Hongo, Bunkyo-ku, Tokyo 113-0033, Japan

Received 17 March 2023 / Accepted 17 July 2023

ABSTRACT

We report the results obtained from *XMM-Newton* observations of the TeV-detected supernova remnant (SNR) HESS J1534-571. We focus on the nature of the cosmic-ray particle content in the SNR, which is revealed by its γ-ray emission. No signatures of X-ray synchrotron emission were detected from the SNR. This is consistent with earlier results obtained with *Suzaku* from other regions of the object. A joint modeling of the *XMM-Newton* and *Suzaku* spectra yields an upper limit for the total X-ray flux from the SNR area of $\sim 5.62 \times 10^{-13}$ erg cm^{-2} s^{-1} (95% C.I.) in the energy band of 2.0–10.0 keV for an assumed photon index of 2.0. On the other hand, we do find evidence in the *XMM-Newton* data for a line-like emission feature at 6.4 keV from localized regions, again confirming earlier *Suzaku* measurements. We discuss the findings in the context of the origin of the observed γ-ray emission. Although neither hadronic nor leptonic scenarios can be fully ruled out, the observed line emission can be interpreted as the result of interactions between lower-energy ($\sim$ MeV) cosmic-ray protons with high gas-density regions in and around HESS J1534-571, and thus potentially be associated with particles accelerated in the SNR.

Key words. gamma rays: ISM – astroparticle physics – ISM: supernova remnants – cosmic rays – X-rays: individuals: HESS J1534-571

1. Introduction

Supernova remnants (SNRs) are generally considered the most relevant sources of energy input for Galactic cosmic rays (CRs) (Ginzburg & Syrovatskii 1964; Hillas 2005). The main arguments are the required kinetic energy per unit time, and the fact that diffusive shock acceleration (Bell & Lucek 2001; Bell 2004) is a well-established particle acceleration mechanism, in agreement with many observational parameters (Blandford & Eichler 1987; Malkov & Drury 2001; Jones & Ellison 1991). A quantitative probe of this scenario is the electromagnetic emission from the accelerated particles in and around the sources. To specifically probe the high end of the leptonic particle spectra, X-ray synchrotron and TeV γ-ray inverse Compton (IC) emission are the relevant channels (Reynolds 1998). The hadronic component, which is energetically relevant from the CR standpoint, can only be probed in γ-rays (through the π^0 decay process), with the high end of the spectrum at TeV-PeV photon energies (Sturner et al. 1997; Drury et al. 1994).

Young SNRs with ongoing particle acceleration toward the highest energies are key targets for the study of CR acceleration, specifically because the escape of particles upstream of the forward shock plays a strong role in modifying the particle spectrum soon after the shock is slowing down. However, the typically high synchrotron fluxes and the lack of spectra extending to $\sim$100 TeV are the motivation for the preference for a leptonic interpretation of the γ-ray spectra in several cases, despite the need to invoke low magnetic fields in the bulk of the emission regions (well below the $\sim$100 μG levels needed for efficient highest-energy particle acceleration, Hillas 2005). TeV-selected SNRs, which should still be (moderately) young given their TeV dominance and by definition presenting low levels of synchrotron emission, are therefore important targets in view of a potential hadronic dominance of the γ-ray emission, which would permit a direct view of the hadronic energetics of the objects.

This motivates a detailed study of HESS J1534-571 as presented in this paper. HESS J1534-571 is one of only three objects that were classified as SNR candidates after their discovery in TeV γ-rays based on a morphological characterization of new objects discovered in the High Energy Spectroscopic System (H.E.S.S.) Galactic plane survey (H.E.S.S. Collaboration 2018a). From the subsequent identification with the SNR candidate SNR G323.7–1.0 found in archival radio continuum data from the Molonglo Galactic Plane Survey (MGPS; Green et al. 2014), HESS J1534-571 was then classified as a confirmed SNR. No clear X-ray counterpart of the SNR shell has been found so far, with the best limits for the nonthermal X-ray emission obtained with *Suzaku* (Mitsuda et al. 2007) observations of a fraction of the shell, yielding 2.4×10^{-11} erg cm^{-2} s^{-1} in the energy band 2.0–12.0 keV assuming a power-law model of index 2 and scaling to the full SNR area (H.E.S.S. Collaboration 2018a). The object has a diameter of $\sim$0.8° and requires several pointings of current (e.g., the X-ray Multi-Mirror Mission, *XMM-Newton*, Aschenbach et al. 2000) or recent X-ray (e.g., *Suzaku*) satellites

for full coverage. Here, we present results obtained from a ∼25 ks *XMM-Newton* pointing covering the previously unobserved part of the SNR. Similar to the *Suzaku* observations that covered the other parts of the shell, no evidence for X-ray synchrotron emission is found. Using both data sets together, we obtain robust constraints on the X-ray emission from the entire shell for the first time, and we discuss the results in the context of the origin of the observed γ-ray emission from the object.

In addition to synchrotron emission from relativistic electrons and plasma emission (bremsstrahlung and thermally excited fluorescence emission lines), cold gas can also give rise to fluorescence lines in X-ray spectra of SNRs. This process occurs when low-energy CR protons interact with nearby cool gas, where the collisional excitation is then followed by radiative deexcitation. In particular, the fluorescence yield of neutral ion (Fe I) for a deexcitation to K-shell transition is 34%, much higher than other atoms such as neutral silicon at 5% or neutral oxygen at 0.8% (Krause 1979; Kallman et al. 2004; Vink 2012). Due to the high fluorescence yield and the relatively high abundance, the Fe Kα line at 6.4 keV is an important diagnostic channel for studying SNRs and the properties of nearby molecular clouds. Evidence for this line has been widely found for different SNRs, such as W28, Kes67, Kes69, Kes78, and W44 (Nobukawa et al. 2018). Saji et al. (2018) reported the existence of such a line in the *Suzaku* observations of HESS J1534-571 at a 4 σ significance level. We have extended the investigation of this line to the *XMM-Newton* data presented in this work.

A search for a possible gas association of the source conducted by Maxted et al. (2018) using Mopra CO Galactic Plane Survey data (Burton et al. 2013) and the Southern Galactic Plane Survey HI data (McClure-Griffiths et al. 2005) indicated that the SNR might be located inside the Scutum-Crux arm and could stem from a core-collapse event at a kinematic distance of ∼3.5 kpc. In this paper, we adopt this distance estimate.

The paper is organized as follows: in Sect. 2 we describe the *XMM-Newton* observations and the data reduction. In Sect. 3 we describe the obtained results and place them in the context of broadband spectral models describing the emission from assumed nonthermal particle populations. The results are further discussed in Sect. 4 and are placed in the context of the results for other SNRs. We conclude with a summary in Sect. 5.

2. Observations and data reduction

The first attempt to observe HESS J1534-571 with *XMM-Newton* (Lumb et al. 2012) was cancelled due to the outburst of a transient source in the field of view. Close to the geometrical center of HESS J1534-571, a previously unknown X-ray binary (XRB) was discovered with the MAXI/GSC instrument in 2017 (Negoro et al. 2017) and independently with *Swift*/BAT (Kostrzewa-Rutkowska et al. 2017), named MAXI J1535-571. Because the distances are uncertain, an association between the two objects can neither be claimed nor be disputed at the moment. Observationally, when the XRB is in outburst, *XMM-Newton* observations of the SNR shell are impossible because the wings of the point spread function (psf) pollute the entire European Photon Imaging Camera (EPIC) field of view (FoV). Therefore, observations that had been approved for 2017 had to be called off, and we were only able to obtain observations in 2020. The parameters of the *XMM-Newton* observation of HESS J1534-571 are shown in Table 1.

For the data reduction, we used the *XMM SAS* software version 20201028_0905-19.0.0. In particular, the work package *XMM-Newton* Extended Source Analysis Software (XMM-ESAS) was employed. In order to obtain images and spectra of the source, we followed the standard steps as recommended in the XMM-ESAS cookbook[1].

Table 1. *XMM-Newton* and *Suzaku* data.

Observation ID	Dates	Exposure time (ks)	Instruments
		24.07	MOS1
0841440101	2020-Mar.-03	24.51	MOS2
		17.07	PN
508013010	2013-Sep.-08	36.9	XIS0-3
508014010	2013-Sep.-09	36.9	XIS0-3
508015010	2013-Sep.-09	36.9	XIS0-3
508016010	2013-Sep.-10	36.9	XIS0-3

First, the standard reprocessing was applied using the ESAS task *epchain, emchain*. The events were then filtered for soft proton flares, and at the same time, assorted diagnostic files were created using *pn-filter, mos-filter* with the default criteria. The MOS CCDs were operated in full-frame mode. After examining the CCDs for their anomalous states, we excluded CCD 3 and CCD 6 of EPIC MOS1 from the analysis. MOS1 CCD 6 was lost due to the micrometeorite strike in March 2005, and MOS1 CCD 3 was damaged in December 2012. Point sources were listed for later removal from the entire FoV using the task *cheese*, applying a flux threshold at 1×10^{-14} ergs cm^{-2} s^{-1}.

Consequently, spectra, response files, and the model particle background spectra and images were produced with the use of the filter-wheel-closed (FWC) data via the tasks *pn-spectra, mos-spectra*. Finally, tasks *pn_back, mos_back* were run to create quiescent particle background files. The pipeline makes use of the data from unexposed corners of the cameras, FWC data as well as the *ROSAT* All-Sky Survey, in order to estimate the contribution of CRs (Kuntz & Snowden 2008). The spectra were then grouped by the HEASOFT FTOOLS command *grppha*, with 50 counts per bin at least. The coverage areas of each instrument were calculated by the task *proton_scale*. The spectral analysis was carried out with the *xspec* software version 12.11.1b.

The *XMM-Newton* images presented in this work are vignetting corrected, background subtracted, and point-source removed. After the initial screening and filtering, residuals from the soft proton contamination might still be present in the images and spectra. In order to take these soft proton residuals into account in addition to the models that represent the main spectra, we added a power-law model that was not folded with the instrumental effective areas. The best-fit parameters for the soft-proton contamination were used to create soft-proton images that were subtracted from the final images. For each energy band, the images from individual instruments were combined and smoothed adaptively.

For the purpose of producing an image in a narrow band around 6.4 keV covering the entire source, we also reprocessed the archival *Suzaku* data taken of HESS J1534-571. *Suzaku* was pointed toward the northern and eastern part of the source in four dedicated observations of approximately 40 ksec each in 2013 (Saji et al. 2018). We employed the HEASOFT software version 6.24, *Suzaku* reprocessing version 3.0.22.44, and the remote calibration files to ensure that we had access to the most current calibration tools. We filtered bad pixels, excluded the

[1] https://heasarc.gsfc.nasa.gov/docs/xmm/esas/cookbook/xmm-esas.html

data from the chip corners, combined 3×3 and 5×5 modes where possible, and excluded data with an elevation <5 deg above Earth or <20 deg above the sunlit limb of Earth. Additional event filtering was applied for XIS0 due to the area discrimination after the XIS0 anomaly in 2009. For the spectral analysis, the ancillary response files (ARF) and redistribution matrix files (RMF) were created using the tasks *xissimarfgen* and *xisrmfgen*, respectively. For the image production, the non-X-ray background within 300 days from the observation was derived by the task *nxbgen* for background subtraction. A simulated exposure map was also created via the task *xissim* for vignetting correction. The individual images from XIS0, XIS1, and XIS3 were rebinned with 8×8 pixels and combined using *ximage*. For images above 5 keV, only the front-illuminated CCDs XIS0 and XIS3 were used because the signal-to-noise ratio of the back illuminated XIS1 is lower at this energy range. The spectra were extracted from the enhanced regions in the 6.3–6.5 keV narrow-band image that were found both by Saji et al. (2018) and in this work. The NXB spectra were calculated using data within ±300 days from the observation day. Similar to *XMM-Newton*, the *Suzaku* spectral analysis was made using the software *xspec*. For reference, Fig. 1 shows the TeV contours of HESS J1534-571 (H.E.S.S. Collaboration 2018a) and the outer boundary of the radio shell G323.7-1.0 discovered in MGPS data (Green et al. 2014), as well as the EPIC and X-ray Imaging Spectrometer (XIS) FoVs of the *XMM-Newton* pointing and the archival *Suzaku* pointings (Saji et al. 2018), respectively.

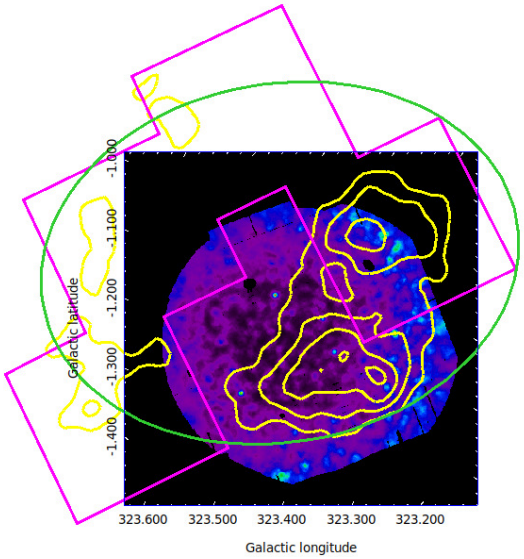

Fig. 1. Adaptively smoothed *XMM-Newton* image in the energy band 2.0–5.0 keV of HESS J1534-571. The green ellipse shows the radio boundary, the magenta region indicates the four *Suzaku* poitings, and the yellow lines represent the TeV surface brightness contour.

3. Results

3.1. X-ray continuum emission

To investigate the potential continuum emission from HESS J1534-571, we produced coadded images from all three *XMM-Newton*-EPIC cameras in two energy bands (the same as were used in Saji et al. 2018), namely a soft band at 0.5–3.0 keV and a hard band at 5.0–8.0 keV. The former is sensitive to putative thermal emission with typical SNR temperatures, and the latter is suited to search for nonthermal (synchrotron) emission. With the radio SNR boundary as a guideline, roughly 85% of the EPIC FoV covers the SNR, and the rest is outside the SNR and can serve as reference and background region. Close inspection of the *XMM-Newton* images shows that no obvious structure is visible that might be associated with the SNR in thermal or in nonthermal emission.

To be able to compare to spectral models of the broadband nonthermal emission of the SNR (see Sect. 3.3), we derived a flux upper limit in the 2.0–10.0 keV band. As on-source region, we used the part of the SNR as defined by the radio boundary that is covered by the EPIC FoV (see Fig. 1). A background spectrum was derived from a source-free (i.e., outside the radio SNR boundary) patch of the FoV. The CCD chips of MOS1 that were available at the time of the observations do not cover the background control region. Therefore, we used the off-source spectrum of MOS2 as the background spectrum for EPIC MOS1 because the sensitivity and calibration of the two MOS cameras are similar. The resulting systematic errors are minor.

We also employed a simultaneous spectral fitting for data from *XMM-Newton* and *Suzaku*. First, test fits for each individual spectrum from each data set (MOS1, MOS2, PN, and 4 *Suzaku* observations) and each telescope (*XMM-Newton* and *Suzaku*) were performed in order to estimate the reasonable range of fit parameters. Then, we carried out a joint fitting to all the source and background data. The background spectra were extracted from the region outside of the radio boundary. We fit all the spectra to the model, which consists of the astrophysical background, and for *XMM-Newton* data an additional, not ARF-folded model for any residual soft proton contamination. We chose the energy range of 1.0–7.0 keV because above 7 keV, the count rate is low. The model for the simultaneous fit is then a collisionally ionized diffuse gas *apec* at a plasma temperature of 0.1 keV to represent the local hot bubble, an absorbed power law *TBabs*pow* with an index of 1.46 for the unresolved cosmic X-ray background, and another absorbed *TBabs*apec* at 0.65 keV for the interstellar medium (ISM). The temperature of the ISM was obtained from earlier test fits and was then fixed. After the best fit was achieved, we fixed the best-fit values and added an absorbed power law *TBabs*pow* model to represent the undetected X-ray source and its total absorption. Because the relevant absorption to the object distance is not known, we adopted the column density through the entire Galaxy estimated by the HEASoft NH FTOOL (HI4PI Collaboration 2016) for the assumed emission component from the SNR. The derived upper limit is therefore a conservative estimate, but the impact is small given the fitted energy range above 2 keV. The data and best-fit models are plotted in Fig. 2. The total models (plotted as solid lines) show the base model without the power-law component, which indicates the upper limit of the synchrotron emission. The spectra of the background control regions are not plotted for better visual presentation.

The power law represents the expected spectral shape of the synchrotron emission in the considered energy range. We adopted two power-law indices: a generic 2.0 value, and a much softer value of 3.0, which corresponds to the average photon index of the model prediction by Araya (2017). Finally, we report the 95% confidence level flux for this additional power-law component and extrapolate into the range 2.0–10.0 keV as the flux upper limit from the covered fraction of the SNR (724.84 arcmin^2 for the *XMM-Newton* FoV and 1214.4 arcmin^2 for *Suzaku* FoV). To be able to compare to model expectations, this limit needs to be extrapolated to the area of the entire SNR defined by the radio region (1521.94 arcmin^2). Assuming that the surface brightness of the SNR is the same (or lower) in the areas that are not covered,

Table 2. Results of the upper-limit estimation.

Region	Radio boundary		TeV peak		*XMM-Newton*	
Index	$\Gamma = 2$	$\Gamma = 3$	$\Gamma = 2$	$\Gamma = 3$	$\Gamma = 2$	$\Gamma = 3$
UL_{2-10}	5.62	4.94	1.03	1.00	2.52	2.27
$\chi^2_{reduced}$	3421/2930	3414/2930	2922/2448	2916/2448	2823/2251	2818/2251

Notes. The upper limit of the flux in the energy range 2.0–10.0 keV is reported in units of $\times 10^{-13}$ erg cm^{-2} s^{-1}. The extraction regions is defined in the text.

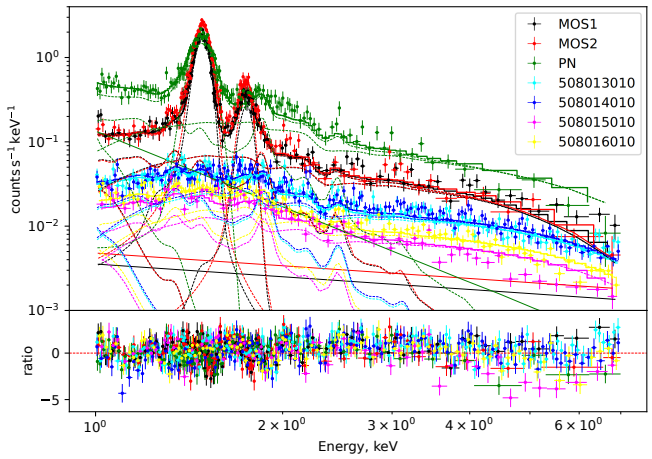

Fig. 2. X-ray spectra of the *XMM-Newton* pointing (MOS1, MOS2, and PN) and the four *Suzaku* pointings in the energy range 1.0–7.0 keV. The upper panel depicts the data and best-fit total model spectrum as well as the individual model components, and the lower panel shows the ratio of each spectrum and the corresponding best-fit model.

a plain area-scaling can be adopted, that is, the relative error on the uncertainty of the zero flux level remains the same. We simply scaled the flux density to the area of the radio boundary. A flux upper limit derived from *XMM-Newton* data alone, representing the flux coming from the SNR's fraction covered by the *XMM-Newton* FoV, is also shown for reference. These two extraction areas are called radio boundary and *XMM-Newton*, respectively (see Table 2).

To test the robustness of the result, we also used a narrower region around the peak significance region of the TeV emission to extract an on-source spectrum because the X-ray emission may trace the gamma-ray emission region better than the entire SNR. This extraction area is referred to as the TeV peak. The derived limits are compared in Table 2. As reference result, we chose the limit obtained for the radio SNR area with an index of 2.0, which yields an upper limit of 5.62×10^{-13} erg cm^{-2} s^{-1} at a 95% confidence level. To place this number in context, the expected flux in a model by Araya (2017) is 2.7×10^{-14} erg cm^{-2} s^{-1} in the 2.0–10.0 keV energy band. The expectation critically depends on the adopted energy cutoff of the electron spectrum population, which was constrained in a leptonic model by fitting to the GeV-TeV (and radio) data from the source. Further comparisons to synchrotron and broadband model expectations are discussed in Sect. 3.3.

3.2. 6.4 keV line emission

Triggered by the report by Saji et al. (2018), we also created an image in the narrow band around 6.3–6.5 keV. The authors reported evidence for line emission at 6.4 keV in the four *Suzaku* pointings on HESS J1534-571 at a statistical significance of $\sim 4\sigma$.

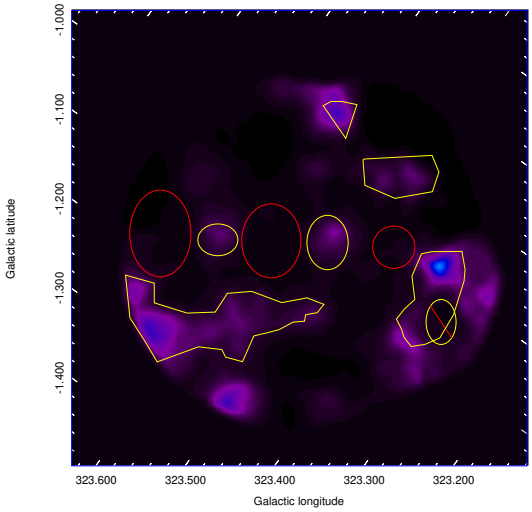

Fig. 3. Adaptively smoothed MOS1-MOS2-PN combined *XMM-Newton* image in the energy band 6.3–6.5 keV of HESS J1534-571. The enhanced and reference regions of MOS1 are depicted with yellow and red boundaries, respectively. The regions differ slightly for different cameras due to their CCD geometry.

The corresponding narrow-band *XMM-Newton* image also shows evidence for localized emission from the area of the SNR. We chose on-source extraction regions based on the enhancements in the image, and reference background regions (Fig. 3). The coadded on- and off-source spectra are shown in Fig. 4 in an energy band between 6.3 and 6.5 keV.

Galactic ridge (Galactic ridge X-ray emission, GRXE; Yamauchi et al. 2016) is expected to be seen from the direction of HESS J1534-571 because the SNR resides in the Galactic plane. These are unresolved X-ray emission lines along the Galactic plane, namely the neutral iron Fe I Kα, Fe XXV Kα, Fe XXVI Kα, and Fe I Kβ centered at 6.4 keV, 6.68 keV, 6.97 keV, and 7.06 keV, respectively. The stacked spectrum from MOS1 and MOS2 data shows that the Fe Kα line emission 6.68 keV from the GRXE is visible in both on-source and off-source spectra at the same level. The Fe XXVI Kα line is also detected at 6.97 keV. The enhancement in the image clearly corresponds to a line-like feature at 6.4 keV, which can be identified with Fe Kα emission, and which is not seen in the reference region. We fit the spectra in the range 5.5–7.5 keV to a power-law component and four Gaussian lines representing the GRXE (Fig. 4).

Similar to Saji et al. (2018), we fixed the Gaussian width of the line 6.68 keV at 23 eV (Koyama et al. 2007) and linked the normalization of the line 7.06 keV as 0.125 times that of the 6.4 keV line (Kaastra & Mewe 1993). The best-fit parameters are shown in Table 3. We ran MCMC simulations to calculate the probability that the 6.4 keV line could stem from background fluctuations. To do this, 1.000 spectra in the energy range of interest were simulated. We found that the 6.4 keV emission is significant at the $\sim 3\sigma$ confidence level and contains the signal from interactions of CRs with cold gas, as well as a small contribution (not significantly detected in the reference region) from the GRXE. Because the extraction regions had to be chosen based on the low-significance image, this is a pre-trial significance. However, taking the significances from the *Suzaku* and the *XMM-Newton* results together, we consider the results summarized above as a sufficient motivation for further investigation of this feature. Because the conversion factor from count rates into flux in this band is very similar between the used *XMM-Newton* and *Suzaku*

Table 3. Best-fit parameters of the spectra analysis of the 6.4 keV clumps.

Parameters	Enhanced region	Reference region
Energy (keV)	6.4 (fixed)	6.4 (fixed)
σ (keV)	0 (fixed)	0 (fixed)
Normalization$^{(a)}$	$1.892^{+1.017}_{-0.959}$	<0.679
Equivalent width$^{(b)}$	549	212
Energy (keV)	6.68 (fixed)	6.68 (fixed)
σ (keV)	0.023 (fixed)	0.023 (fixed)
Normalization	$1.096^{+1.121}_{-0.811}$	$0.762^{+0.785}_{-0.628}$
Equivalent width	275	504
Energy (keV)	6.97 (fixed)	6.97 (fixed)
σ (keV)	0 (fixed)	0 (fixed)
Normalization	$0.157^{+1.352}_{-0.106}$	<0.578
Equivalent width	224	172

Notes. Errors and upper limits are given at 90% C.L. $^{(a)}$Photon flux in units of 10^{-5} photons cm^{-2} s^{-1}, $^{(b)}$keV at a 95% significance level.

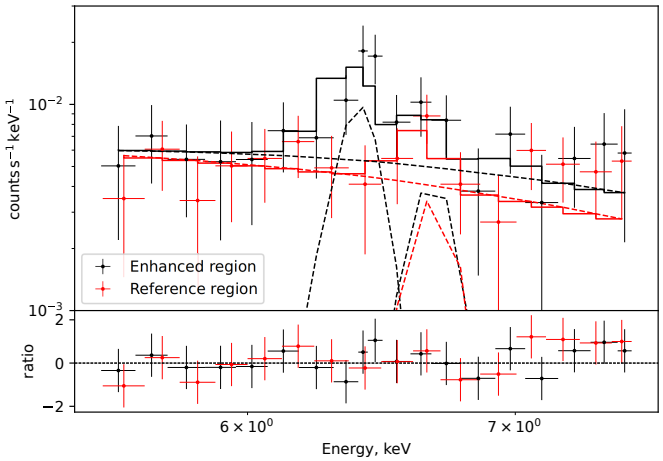

Fig. 4. MOS1+MOS2 stacked spectra and the best-fit model of the 6.4 keV enhanced region (black) and of the reference region (red).

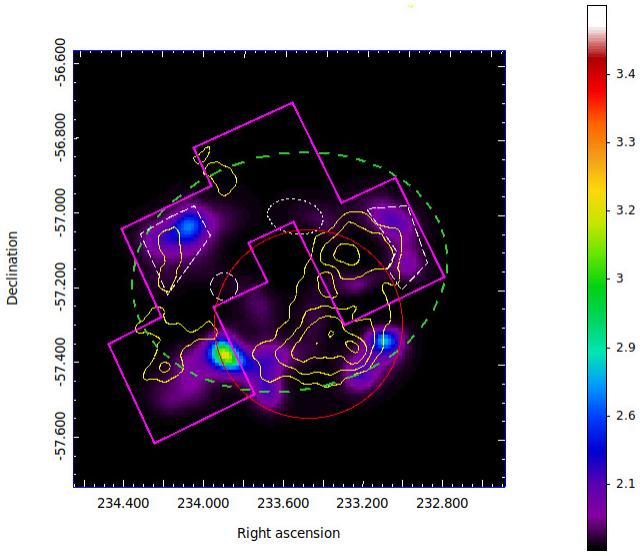

Fig. 5. Combined *XMM-Newton* and *Suzaku* image of HESS-J1534-571 in 6.3–6.5 keV in units of counts per second. The red circle shows the *XMM-Newton* field of view, the green ellipse indicates the *Molonglo* radio boundary, the yellow contour follows the TeV profile, and the magenta region shows the four pointings of the *Suzaku* observations. The dashed white regions denote the enhancement regions found by Saji et al. (2018). A point source in the Suzaku southern pointing has been removed. A similarity between the bright clumps in this narrow energy band and the TeV profile is apparent.

detectors (MOS1+2 and XIS0+3, respectively), we combined the count maps of these two instruments to show the morphology of the enhanced Fe Kα line emission across the complete SNR. Figure 5 shows a mosaic of *XMM-Newton* and *Suzaku* pointings in the 6.3–6.5 keV band, with the radio boundary and the TeV emission overlaid as contours. A visual comparison to the *Suzaku* map in Saji et al. (2018) reveals overall similar enhancement positions and shapes, despite the limited significance of individual features. Small deviations may be attributed to differences in handling of the area discrimination for the XIS0 chip (lower fluxes in the small dashed circle and ellipse regions in Fig. 5) and in the creation of the exposure map. In the southern *Suzaku* pointing, the difference (apparently higher flux) might be attributed to a different zero suppression in the image, after the necessary point-source subtraction.

3.3. Broadband SED of HESS J1534-571

With the robust X-ray upper limit of the entire SNR obtained in this work, we investigated whether the relativistic particle distribution in the SNR can be further constrained through its expected emission. Radio data at 843 MHz come from MGPS, and the flux point needs to be treated as a lower limit because certain angular scales may be missed. Sources with a diameter larger than 25 arcmin are not entirely covered by the radio telescope (Green et al. 2014). The GeV spectrum obtained with Fermi-LAT was taken from Araya (2017). The TeV data from H.E.S.S. were taken from H.E.S.S. Collaboration (2018a). To convert the integral upper limit obtained from the X-ray data into a value suitable for the (differential) SEDs shown in Figs. 6 and 7, we performed a spectral joint fitting of *XMM-Newton* and *Suzaku* in the range 2.0–7.0 keV and extrapolated to 2.0–10.0 keV (Sect. 3.1). The *naima*[2] (Zabalza 2015) package was used to simulate the nonthermal radiation from assumed relativistic particle populations. All models presented here are static one-zone models, in which homogeneous distributions of particles and of target fields relevant for the emission are maintained.

In Fig. 6, we show the result from a leptonic model in which the entire emission across all wavebands is dominated by leptonic emission, electron synchrotron at radio to X-ray frequencies, and IC emission in the GeV to TeV band. The photon fields that are upscattered by the relativistic electrons are the cosmic microwave background (CMB), near-infrared (NIR) stellar emission, and far-infrared (FIR) dust, which can be described by a blackbody distribution. For the NIR field, 3000 K and 0.4 eV cm^{-3} were adopted (Shibata et al. 2010; Vernetto & Lipari 2016), and for the FIR field, we used 20 K and 0.8 eV cm^{-3} (Araya 2017). The distance to the SNR was set to 3.5 kpc, adopting the association with the Galactic arm Scutum-Crux (Maxted et al. 2018). Because an unbroken power law was adopted for the particle population, the adopted magnetic field needed to be lower than 10 μG in order not to undershoot the radio lower limit and overshoot the γ-ray data. ∼10 μG would be required in simple shock-compression scenarios, and this value was also found by

[2] https://naima.readthedocs.io/en/latest/api-mcmc.html

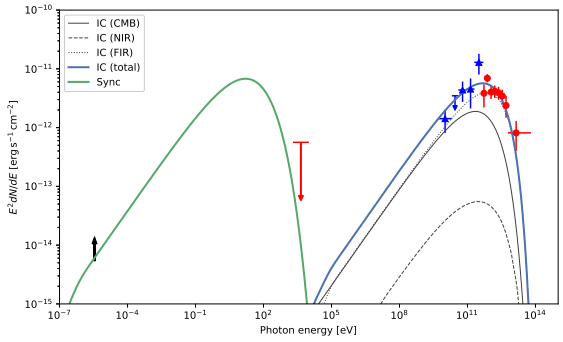

Fig. 6. Spectral energy distribution of HESS J1534-571. The *Fermi*-LAT data (Araya 2017) are plotted as blue tirangles. The red circles are H.E.S.S. TeV flux points (H.E.S.S. Collaboration 2018a). The black arrow shows the lower limit of the flux detected in radio (Green et al. 2014). The red arrow illustrates the estimated upper limit in the 2.0–10.0 keV band. The leptonic model described in the text is also plotted.

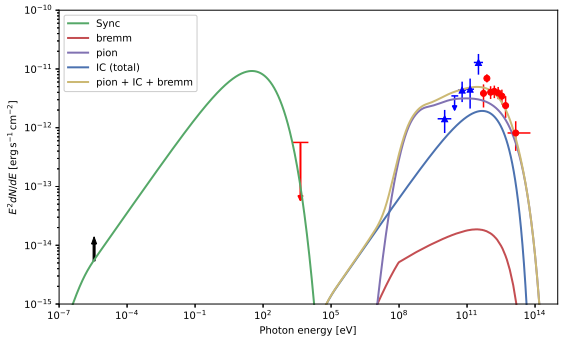

Fig. 7. Data points are same as in Fig. 6, here compared to the hadronic model described in the text.

Ferriere (2009), for example, even for the diffuse intercloud medium. Here, we adopted 6 μG (Araya 2017). To match the γ-ray spectral shape, a particle cutoff energy at 7 TeV and a spectral index of 1.9 were chosen. The gas density was assumed to be low so that bremsstrahlung could be ignored; it is usually assumed that if Bremsstrahlung plays a significant role in the γ-ray range, corresponding line emission in the X-ray band should be visible. This model satisfies all data, including the upper limit derived in X-rays.

Triggered by the low required magnetic field in the leptonic model, which speaks against recent TeV particle acceleration, and by the Fe Kα-indications of lower-energy protons in the SNR, we also attempted to fit a hadronic emission model to the broadband data. Here, the leptonic population was only constrained by the radio to X-ray band, except for the magnetic field. In this case, we used 12 μG in order to follow the radio lower limit and at the same time reduce the contribution of IC emission in the very high energy range. Canonically, the proton particle distribution is described with a power law with an energy index of 2.0 (in the test-particle approach of a Fermi-accelerated spectrum), or softer when particle escape is relevant, for instance. We show a model with an index of 2.0 and a cutoff energy at 60 TeV in Fig. 7. The input for the synchrotron and IC radiation were the same as for the leptonic model. The hadronic model requires the energy of the accelerated protons to be no more than a few 10^{50} erg (Aharonian & Atoyan 1999). We assumed two different values of the ISM density at 0.5 cm^{-3} and 1 cm^{-3} (Fig. 7), which correspond to the total energy of the protons at 3.3×10^{50} erg and 1.6×10^{50} erg, respectively. These densities could be viable in a scenario in which the emission occurs in molecular clouds or in gas shells created by the progenitor wind. At this level of target gas density, the contribution of bremsstrahlung emission is negligible.

4. Discussion

A pure leptonic model describes all available data from HESS J1534-571 well. The model is very similar to the one proposed by Araya (2017). Because of the relatively low energy of the particle spectral cutoff and the large size of the remnant, which leads to a sensitivity in the X-ray band that is lower by some orders of magnitude compared to typical point-source sensitivities, the X-ray limit obtained in this work is not sufficient to challenge a pure leptonic model. The low deduced magnetic field implies that the bulk of emission occurs outside of shock-acceleration regions. This is reminiscent of relic TeV pulsar wind nebulae, which also have no morphologically matching counterpart in X-rays (Kargaltsev et al. 2012; H.E.S.S. Collaboration 2018b). The fact that no X-ray synchrotron emission is detected even from the actual accelerating sites (possibly at the forward shock as outlined by the radio remnant) can be explained by shocks that have meanwhile slowed down, which implies that the corresponding high-energy end of the synchrotron spectrum has shifted to lower energies to which X-ray satellite observations are not sensitive (Vink 2012). Alternatively, the flux level at these sites could be too low for the current detectors because of the large angular extension of the source.

The alternative, hadronic scenario for the γ-ray emission matches the available γ-ray data less well in the simple test-particle and one-zone form as presented in Fig. 7. It might require modifications. The γ-ray spectral shape is reminiscent of the shape of RX J1713.7-3946 (Muraishi et al. 2000). For this SNR, motivated by the excellent morphological match between TeV emission and gas tracers (Sect. 3.2), a scenario has been proposed in which the energy-dependent penetration depth of CR protons into dense clumpy molecular clouds leads to a strong modification of the spatially integrated γ-ray spectrum (Aharonian et al. 2006; Gabici & Aharonian 2014). Because the highest-energy protons "see" denser material, the emission is boosted, which leads to a steepening of the spectrum below the cutoff energy. A spectrum like this would match the observed γ-ray data from HESS J1534-571 qualitatively better. This scenario would imply that the MeV/GeV emission would differ from the TeV emission spatially, which cannot be probed with the currently available γ-ray data from Fermi-LAT. However, if the Fe Kα emission tentatively detected from HESS J1534-571 is taken as a tracer of low-energy CRs, then the apparent morphology seen in Fig. 5 is agrees with expectations qualitatively. The Fe Kα-emission is on the scale of the SNR size following the TeV emission, but on smaller angular scales, the agreement appears to be poor. Moreover, this hadronic scenario would imply dense molecular clumps in spatial correspondence to the TeV emission, and indeed, Maxted et al. (2018) have identified molecular clumps like this in CO emission, following the TeV emission morphology on the scale of the full SNR. However, given the low statistical significance of individual morphological features both in the TeV and the X-ray band, any firm conclusion needs to be corroborated by future more sensitive observations.

If the Fe Kα line at 6.4 keV indeed stems from CR protons interacting with gas material (at typical particle energies of 100 MeV), a correlation between the GeV luminosity and the 6.4 keV line luminosity would be expected, not only on smaller

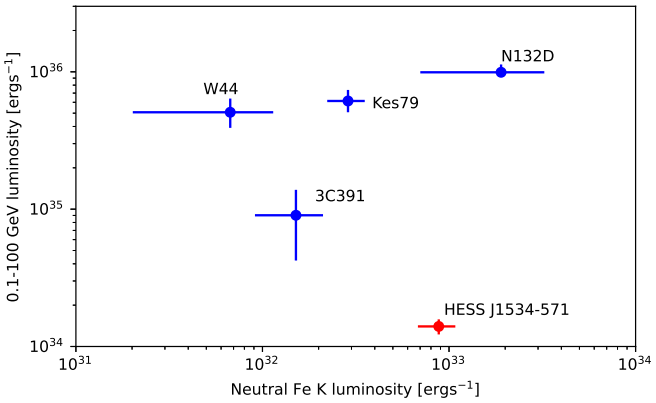

Fig. 8. Relation of the Fe Kα line emission luminosity and the luminosity in the range of 0.1–100 GeV γ-ray detection. The red data point shows HESS J1534-571 (Fe Kα: this work, GeV: Araya 2017), and the blue points represent N132D, Kes79, W44, and 3C391 (Bamba et al. 2018; Acero et al. 2016; Sato et al. 2016).

morphological scales in an individual SNR, but also on average for all SNRs for which the γ-ray emission is suspected to be of hadronic nature. Figure 8 shows such a correlation plot, in which we compare the data from HESS J1534-571 to numbers from other SNRs (taken from Bamba et al. 2018). To derive the line luminosity for HESS J1534-571, we simply added the line fluxes from *XMM-Newton* ($1.9 \pm 1.0 \times 10^{-5}$ photons cm^{-2} s^{-1}, see Table 3) and from *Suzaku* ($4.0 \pm 0.9 \times 10^{-5}$ photons cm^{-2} s^{-1} derived from the enhanced regions in our analysis) because the corresponding extraction areas overlap very little. The statistical uncertainties of the Fe line luminosities were calculated from the respective photon flux errors at the 90% confidence level (Bamba et al. 2018; Auchettl et al. 2014). The statistical uncertainties of the GeV luminosities were derived from the Fermi-LAT analysis of each SNR (W44, Abdollahi et al. 2022; Kes 79, Auchettl et al. 2014; N132D, Bamba et al. 2018; 3C391, Castro & Slane 2010; HESS J1534-571, Araya 2017). We again adopted the distance of 3.5 kpc following the Scutum-Crux arm gas association in Maxted et al. (2018) for HESS J1534-571. The figure shows, however, that no clear conclusion can be drawn for HESS J1534-571 from this comparison at this point in time. While the Fe Kα luminosity is similar to that of the other SNRs, the GeV luminosity is substantially lower. A corresponding lack of dense molecular clouds in the environment may also limit the intensity of the 6.4 keV line. If confirmed, this would indicate a different physical mechanism for the production of the Fe Kα line emission.

5. Conclusion

For the first time, a TeV-emitting SNR has been shown to not exhibit a clear X-ray continuum counterpart at the current X-ray satellite sensitivity. This is a quite robust statement because the *XMM-Newton* and *Suzaku* observations together cover ~85% of the radio shell.

The γ-ray data of HESS J1534-571 can be explained in a leptonic emission scenario, with a magnetic field that indicates that the γ-ray emitting electrons have propagated away from their acceleration sites, similar to relic TeV pulsar wind nebula scenarios. A hadronic emission scenario can be constructed under the assumption that the spectrum is modified by energy-dependent penetration of the accelerated protons into dense and clumpy gas material. This scenario also avoids a potential conflict with the lack of thermal X-ray emission from the SNR. We find evidence for Fe Kα emission from localized regions in the SNR, confirming earlier findings of Saji et al. (2018). Whether this emission is caused by interactions of low-energy CRs in the SNR and thus could support a hadronic nature of the γ-ray emission requires further investigations with more sensitive next-generation instruments.

Acknowledgement. We thank the anonymous referee and editor for the valuable comments and suggestions. We acknowledge support from the Deutsches Zentrum für Luft- und Raumfahrt (DLR) through DLR-PT grant FKZ 50 OR 1914. This work is based on observations obtained with *XMM-Newton*, an ESA science mission with instruments and contributions directly funded by ESA Member States and NASA. This research has also made use of data obtained from the *Suzaku* satellite, a collaborative mission between the space agencies of Japan (JAXA) and the USA (NASA).

References

Abdollahi, S., Acero, F., Baldini, L., et al. 2022, ApJS, 260, 53
Acero, F., Ackermann, M., Ajello, M., et al. 2016, ApJS, 224, 8
Aharonian, F. A., & Atoyan, A. M. 1999, A&A, 351, 330
Aharonian, F., Akhperjanian, A. G., Bazer-Bachi, A. R., et al. 2006, A&A, 449, 223
Araya, M. 2017, ApJ, 843, 12
Aschenbach, B., Briel, U. G., Haberl, F., et al. 2000, SPIE Conf. Ser., 4012, 731
Auchettl, K., Slane, P., & Castro, D. 2014, ApJ, 783, 32
Bamba, A., Ohira, Y., Yamazaki, R., et al. 2018, ApJ, 854, 71
Bell, A. R. 2004, MNRAS, 353, 550
Bell, A. R., & Lucek, S. G. 2001, MNRAS, 321, 433
Blandford, R., & Eichler, D. 1987, Phys. Rep., 154, 1
Burton, M. G., Braiding, C., Glueck, C., et al. 2013, PASA, 30, e044
Castro, D., & Slane, P. 2010, ApJ, 717, 372
Drury, L. O., Aharonian, F. A., & Voelk, H. J. 1994, A&A, 287, 959
Ferriere, K. 2009, A&A, 505, 1183
Gabici, S., & Aharonian, F. A. 2014, MNRAS, 445, L70
Ginzburg, V. L., & Syrovatskii, S. I. 1964, The Origin of Cosmic Rays (New York: Macmillan)
Green, A., Reeves, S., & Murphy, T. 2014, PASA, 31
H.E.S.S. Collaboration (Abdalla, H., et al.) 2018a, A&A, 612, A8
H.E.S.S. Collaboration (Abdalla, H., et al.) 2018b, A&A, 612, A2
HI4PI Collaboration (Ben Bekhti, N., et al.) 2016, A&A, 594, A116
Hillas, A. M. 2005, J. Phys. G Nucl. Phys., 31, R95
Jones, F. C., & Ellison, D. C. 1991, Space Sci. Rev., 58, 259
Kaastra, J. S., & Mewe, R. 1993, A&AS, 97, 443
Kallman, T., Palmeri, P., Bautista, M., Mendoza, C., & Krolik, J. 2004, ApJS, 155, 675
Kargaltsev, O., Pavlov, G. G., & Durant, M. 2012, in Electromagnetic Radiation from Pulsars and Magnetars, eds. W. Lewandowski, O. Maron, & J. Kijak, Astronomical Society of the Pacific Conference Series, 466, 167
Kostrzewa-Rutkowska, Z., Lopez, K. M., Jonker, P. G., et al. 2017, ATel, 11007, 1
Koyama, K., Hyodo, Y., Inui, T., et al. 2007, PASJ, 59, 245
Krause, M. O. 1979, J. Phys. Chem. Ref. Data, 8, 307
Kuntz, K., & Snowden, S. 2008, A&A, 478, 575
Lumb, D. H., Schartel, N., & Jansen, F. A. 2012, Opt. Eng., 51, 011009
Malkov, M. A., & Drury, L. O. 2001, Rep. Progr. Phys., 64, 429
Maxted, N. I., Braiding, C., Wong, G. F., et al. 2018, MNRAS, 480, 134
McClure-Griffiths, N. M., Dickey, J. M., Gaensler, B. M., et al. 2005, ApJS, 158, 178
Mitsuda, K., Bautz, M., Inoue, H., et al. 2007, PASJ, 59, S1
Muraishi, H., Tanimori, T., Yanagita, S., et al. 2000, A&A, 354, A57
Negoro, H., Ishikawa, M., Ueno, S., et al. 2017, ATel, 10699, 1
Nobukawa, K. K., Nobukawa, M., Koyama, K., et al. 2018, ApJ, 854, 87
Reynolds, S. P. 1998, ApJ, 493, 375
Saji, S., Matsumoto, H., Nobukawa, M., et al. 2018, PASJ, 70, 23
Sato, T., Koyama, K., Lee, S.-H., & Takahashi, T. 2016, PASJ, 68, S8
Shibata, T., Ishikawa, T., & Sekiguchi, S. 2010, APJ, 727, 38
Sturner, S. J., Skibo, J. G., Dermer, C. D., & Mattox, J. R. 1997, ApJ, 490, 619
Vernetto, S., & Lipari, P. 2016, Phys. Rev. D, 94, 063009
Vink, J. 2012, A&ARv, 20, 49
Yamauchi, S., Nobukawa, K. K., Nobukawa, M., Uchiyama, H., & Koyama, K. 2016, PASJ, 68, 59
Zabalza, V. 2015, in International Cosmic Ray Conference, 34, 922